Nonlinear Analysis of Automotive Hydraulic Engine Mount

Gun Kim
Post-Doctoral
Research Associate.

Rajendra Singh
Professor.
Fellow ASME

Fluid Power Laboratory,
Department of Mechanical Engineering,
The Ohio State University,
Columbus, OH 43210-1107

Nonlinear properties of a generic hydraulic mount with an inertia track are identified and characterized by using experimental and analytical approaches. A low-frequency lumped-parameter mathematical model of the hydraulic mount is developed over 1 to 50 Hz, based on the measured nonlinear system parameters such as the steady-state inertia track fluid resistances and fluid chamber compliances. New experiments specifically designed for this study are also described. The effect of temperature on the mount dynamic properties is discussed briefly. When compared with measured signals under sinusoidal testing conditions, our model predicts time and frequency domain responses reasonably well. One of the reasons for some discrepancies between theory and experiment is attributed to the need for an accurate model describing the gas-liquid phase transformation and cavitation phenomenon.

1 Introduction

1.1 Problem Formulation. During the last decade, several hydraulic mounts have been proposed to control automotive engine vibration and noise problems (Graf and Shoureshi, 1988). It has been found from a few experiments that dynamic properties of the hydraulic mount are significantly frequency-dependent and highly sensitive to deflection amplitude (Corcoran and Ticks, 1984). Therefore, the development of a nonlinear mathematical model is necessary for an improved understanding of the hydraulic mount dynamics and vehicle design studies. While a few investigators have mentioned the nonlinear system parameters of the hydraulic mount, no prior literature exists which rigorously describes the nonlinear dynamics issue. In fact, all of the mathematical models reported in the literature are essentially based on the linear system theory (Flower, 1985; Singh et al, 1992). This situation is slightly different for another hydraulic damping device, the conventional automotive shock absorber. Lang (1977) and Vliet and Sankar (1983) developed nonlinear mathematical models of automotive and motorcycle shock absorbers, respectively. However, the operating frequency range and dynamic characteristics of a typical hydraulic engine mount are considerably different from those of a shock absorber. For instance, a shock absorber makes use of sharp-orifice damping, whereas the damping properties of a hydraulic mount arise from a long orifice or inertia track.

The main objective of this paper is to develop a simplified, yet reasonably accurate, low-frequency nonlinear mathematical model of a hydraulic mount with an inertia track. Specific objectives are as follows: (i) to formulate a nonlinear lumped-parameter model of the governing fluid system; (ii) to identify, measure and characterize nonlinear properties such as chamber compliances and inertia track fluid resistances; (iii) to examine the effects of temperature and fluid phase transformation on the dynamic response; and (iv) to validate the model by comparing predictions with measured data in time and frequency domains over 1 to 50 Hz.

1.2 Example Case. Two key components of a regular hydraulic mount are an inertia track and a decoupler (Singh et al., 1992). However, as shown in Fig. 1, the generic hydraulic mount examined in this study is not equipped with the decoupler in order to clarify the nonlinear fluid system dynamics. The upper and lower chambers are filled with the glycol fluid mixture of anti-freeze and distilled water. The static stiffness $\bar{k}_r$ of the elastomeric body or top element is selected to support

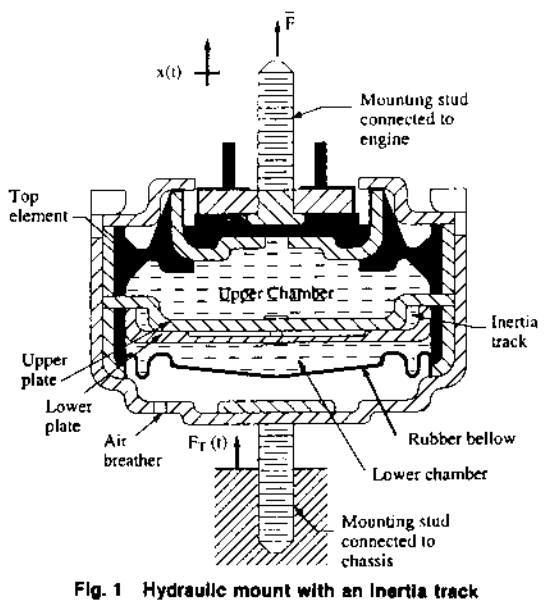

Fig. 1 Hydraulic mount with an inertia track

Contributed by the Dynamic Systems and Control Division for publication in the JOURNAL OF DYNAMIC SYSTEMS, MEASUREMENT, AND CONTROL. Manuscript received by the Dynamic Systems and Control Division, March 16, 1992; revised manuscript received December 10, 1992. Associate Technical Editor: A. Akers.

Singh-064

a portion of the engine weight (i.e., $-\bar{F}$). A cyclic engine motion causes oscillatory fluid flow between two chambers through the inertia track. A four-cylinder engine block is typically attached to the vehicle frame through three or four mounts. However, only the vertical direction is considered in this paper since the emphasis is on the hydraulic mount itself.

Dynamic properties (elastic stiffness and damping) of the hydraulic mount are measured on an electrohydraulic material testing system. A compressive preload $-\bar{F}$ is applied to the mount top element through a hydraulic actuator. In this study, $\bar{F} = -1200$ N. The actuator is then excited with a sinusoidal stroke

$$x(t) = X \sin \omega t \tag{1}$$

under closed-loop control while the dynamic force transmitted to the fixed foundation, F_T, is measured in the steady-state condition. The measured F_T is highly nonsinusoidal for the hydraulic mount. Usual industrial practice is to apply $X \leq 1.0$ mm over 1 to 50 Hz; accordingly, these specifications are adopted for our mathematical simulation.

2 Mathematical Formulation

The inherent nature of the inertia track flow is that it is oscillating turbulent type which does not seem to be amenable to an accurate analysis. Therefore, a lumped-parameter modeling approach is obviously more appropriate for representing the inertia track dynamics and clarifying the dynamic response of the hydraulic mount. The flow velocity in the inertia track is smaller than the acoustic wave velocity of the glycol fluid (≈ 1500 m/s) by two orders of magnitude. As a result, fluid density ($\rho_g = 1059$ kg/m^3) may be taken constant and thermal effects may be neglected (Kirshner and Katz, 1975). Now, since the acoustic wave length of interest is larger than the inertia track length or diameter by at least two orders of magnitude even at 50 Hz, only one lump is employed and its fluid compliance is ignored in this study. Figure 2(*a*) shows the resulting lumped-parameter model of the inertia track mount. Here #11, #12, #21, and #22 are the control volumes just below the top element (#*r*), above the upper plate, below the lower plate, and above the rubber bellow, respectively. And #1, #2, and #*i* are the control volumes for the remaining upper chamber, lower chamber and inertia track, respectively.

2.1 Fluid System Equations. Application of the momentum equation to #1 and #2 yields

$$p_{12}(t) - p_{11}(t) = I_1(t)\dot{q}_1(t) \tag{2}$$

$$p_{22}(t) - p_{21}(t) = I_2(t)\dot{q}_2(t) \tag{3}$$

where p_{11}, p_{12}, p_{21}, and p_{22} are fluid pressures at the ends of #1 and #2, respectively, I_1 and I_2 are time-varying fluid inertances of #1 and #2, respectively, with the total inertance $I_1 + I_2$ being constant, and q_1 and q_2 are volume flow rates corresponding to I_1 and I_2. The governing equation for #*i* may be derived from the first-order fluid system dynamics

$$p_{21}(t) - p_{12}(t) = I_i\dot{q}_i(t) + R_i(\Delta\hat{p}_f, q_i)q_i(t) \tag{4}$$

where I_i is the time-invariant fluid inertance of #*i*, q_i is the volume flow rate through #*i*, $\Delta\hat{p}_f = p_{21} - p_{12}$ is the pressure drop. Here, $R_i(\Delta\hat{p}_f, q_i)$ represents all of the fluid resistances between p_{21} and p_{12} based on the first-order system dynamics, including the minor losses due to sudden contraction and expansion at the inertia track ends.

Volumetric continuity for #11, #12, #21, and #22 yields,

$$q_1(t) - A_p\dot{x}(t) = C_{11}(V_{11}, p_{11})\dot{p}_{11}(t) \tag{5}$$

$$q_i(t) - q_1(t) = C_{12}(V_{12}, p_{12})\dot{p}_{12}(t) \tag{6}$$

$$q_2(t) - q_i(t) = C_{21}(V_{21}, p_{21})\dot{p}_{21}(t) \tag{7}$$

$$-q_2(t) = C_{22}(V_{22}, p_{22})\dot{p}_{22}(t) \tag{8}$$

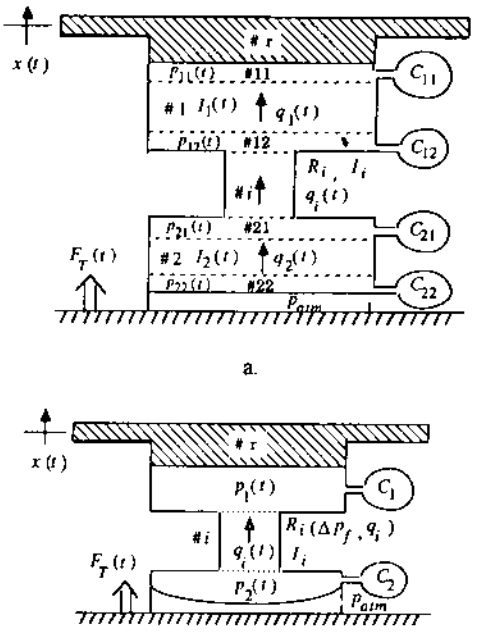

Fig. 2 A lumped-parameter model of hydraulic mount. (*a*) Broadband model; (*b*) reduced-order low frequency model.

where A_p is the equivalent piston area of the top element, $C_{11}(V_{11}, p_{11})$ and $C_{22}(V_{22}, p_{22})$ are the nonlinear compliances of #11 including the top element and #22 including the rubber bellow, and $C_{12}(V_{12}, p_{12})$ and $C_{21}(V_{21}, p_{21})$ are nonlinear compliances of #12 and #21.

2.2 Force Transmitted to the Fixed Frame. Dynamic properties of the top element (#*r*) are represented by the Voigt-type model with frequency-variant elastic stiffness $k_r(\omega)$ and damping coefficient $b_r(\omega)$ in the shear mode. The effect of X on k_r and b_r has been found to be negligible under the typical sinusoidal testing conditions. For the static equilibrium condition (described by an overhead bar) under $\bar{F}$, $\bar{F}_T$ is given as

$$\bar{F}_T = \bar{k}_r\bar{x} + A_p(p_{\text{atm}} - \bar{p}) = \bar{F} \tag{9}$$

where p_{atm} is the atmospheric pressure. Under the dynamic excitation $x(t)$, F_T is

$$F_T(t) = k_r x(t) + b_r\dot{x}(t) + A_p(p_{21}(t) - p_{12}(t) - p_{22}(t) + \bar{p}) \tag{10}$$

2.3 Low Frequency Model. Assuming that the fluid impedances $j\omega I_1$ and $j\omega I_2$ are negligible below 50 Hz, Eqs. (2) and (3) are simplified as follows: $p_{11}(t) = p_{12}(t) = p_1(t)$ and $p_{21}(t) = p_{22}(t) = p_2(t)$. Supposing that $C_{12} = C_{21} = 0$ since C_{11} and C_{22} are more compliant, Eqs. (6) and (7) yield that $q_1(t) = q_i(t) = q_2(t)$. Now denoting $C_1 = C_{11}$ and $C_2 = C_{22}$, we may obtain a low frequency model as shown in Fig. 2(*b*). Its nonlinear governing equations are derived from Eqs. (4), (5), (8), and (10) as follows:

$$p_2(t) - p_1(t) = I_i\dot{q}_i(t) + R_i(\Delta p_f, q_i)q_i(t) \tag{11}$$

$$q_i(t) - A_p\dot{x}(t) = C_1(V_1, p_1)\dot{p}_1(t) \tag{12}$$

$$-q_i(t) = C_2(V_2, p_2)\dot{p}_2(t) \tag{13}$$

$$F_T(t) = k_r x(t) + b_r\dot{x}(t) + A_p(\bar{p} - p_1(t)) \tag{14}$$

where the pressure drop $\Delta p_f = p_2 - p_1$. In order to characterize nonlinear system properties of the hydraulic mount, $C_1(V_1, p_1)$, $C_2(V_2, p_2)$ and $R_i(\Delta p_f, q_i)$ must be measured.

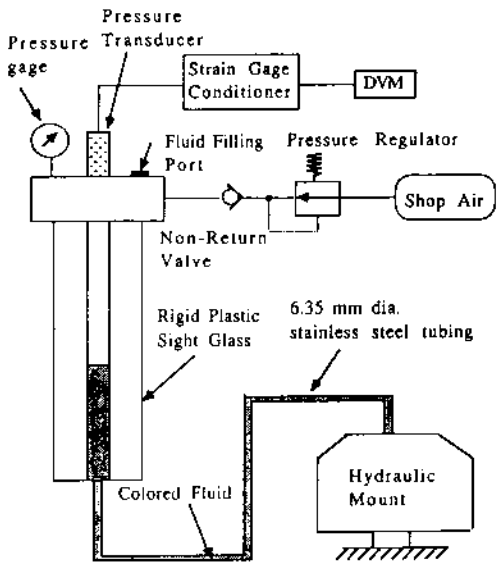

Fig. 3 Measurement setup for nonlinear chamber compliances C_1 and C_2

3 Measurement of Nonlinear System Parameters

3.1 Chamber Compliance. The test setup shown in Fig. 3 is employed to measure the pressure versus volume relationships of upper and lower chambers or to find nonlinear C_1 and C_2. By adjusting the air pressure regulator, chamber pressure is increased by Δp. Subsequently, the chamber volume expands by ΔV, which is measured in terms of the corresponding decrease in the height of colored-liquid level. The measuring length of sight glass is about 9 cm, and measuring diameters are 1.0 cm and 3.0 cm for C_1 and C_2 measurements, respectively. The setup consisting of sight glass, steel tubing and hydraulic mount block is assembled in a liquid bath to keep the air from being entrapped.

The measured data for both chambers are shown in Fig. 4. Their polynomial relationships generated by multiple regression routines (Doebelin, 1980) are as follows:

$$p_1 = -6.4V_1 + 29.2V_1^{7/6} + p_{\text{atm}} \tag{15}$$

$$p_2 = 5.26\times10^{-3}V_2^{2.5} - 8.9\times10^{-8}V_2^6 + 1.41\times10^{-8}V_2^{6.5} + p_{\text{atm}} \tag{16}$$

where p_1 and p_2 are absolute pressures (kPa), V_1 and V_2 are chamber volume increments (cc) from the condition that $p_1 = p_2 = p_{\text{atm}}$. The lower rubber bellow is more compliant than the top element by an order of magnitude although both are produced from the same type of rubber material (duro 51). This is because the lower rubber below is much thinner than the top element, in addition to its geometric effect. Note that $C_1(V_1, p_1)$ and $C_2(V_2, p_2)$ are carefully selected at the manufacturing stage to ensure that balanced damping forces are produced during both upward and downward engine motions.

In practice, the experimental setup of Fig. 3 measures only positive compliance for $p_1 > p_{\text{atm}}$. When $p_1 < p_{\text{atm}}$, there should be a negative compliance of the top element itself; some air initially dissolved in the glycol fluid may be released; the glycol fluid may become a mixture of liquid and gas phases, and further, in extreme cases, vaporous cavitation may occur (Pai, 1977). All of the above-mentioned phenomena which are quantified here by the negative C_1 are difficult to measure and not amenable to accurate analytical predictions. Therefore, in our mathematical model, the negative C_1 is instead simulated by assuming that a small amount of air volume, i.e., $\bar{V}_{\text{air}} = 0.025$ cc, is initially present in the top portion of the upper chamber. Note that $\bar{V}_1$ is 40 cc at the static equilibrium under $\bar{F} = -1200$ N. The negative C_1 characteristics, calculated by using the ideal gas law, are depicted in Fig. 4(*a*).

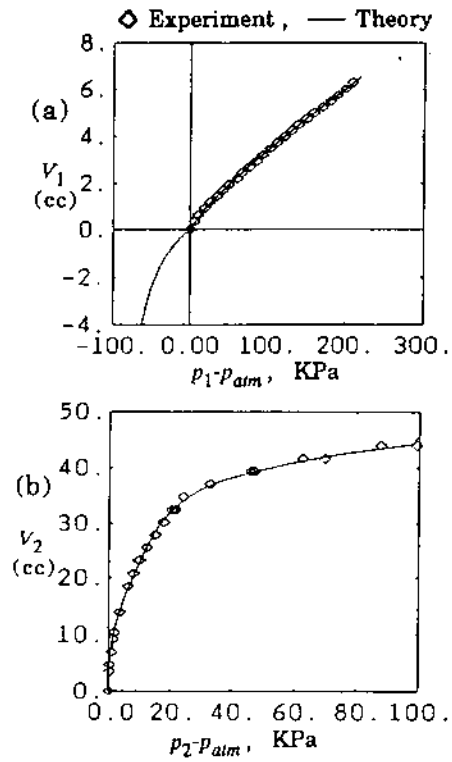

Fig. 4 Measured nonlinear compliance relationships. (*a*) Upper chamber; (*b*) lower chamber.

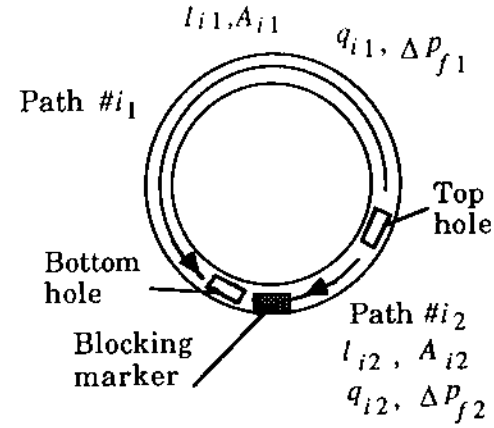

Fig. 5 Two flow paths in the inertia track assembly

3.2 Fluid Resistance of Inertia Track. Since a "small" clearance exists between the blocking marker on the lower plate and the upper plate as shown in Fig. 5, q_i is actually comprised of q_{i1} and q_{i2} through two distinct flow paths $\#i_1$ and $\#i_2$, respectively. Length and cross-sectional are of $\#i_1$ are denoted by l_{i1} and A_{i1}, while l_{i2} and A_{i2} for $\#i_2$. The pressure drops related with q_{i1} and q_{i2} are denoted by Δp_{f1} and Δp_{f2}. Since q_i decreases monotonically beyond a certain resonant frequency ($\approx$ 10 Hz) of the inertia track, the effect of oscillating flow on $R_i(\Delta p_f, q_i)$ is assumed to be insignificant in this study.

The steady-state flow resistances of $\#i_1$ and $\#i_2$ are measured by employing a specially prepared hydraulic circuit, where a centrifugal pump recirculates the glycol fluid flow. An inertia track assembly is incorporated in a take-apart mount block to measure Δp_{f1} and Δp_{f2} for various channel codes (which denote different A_i and l_i) with a differential pressure transducer. Three differnt flowmeters are employed to measure q_i: turbine flowmeter 1 (operating range = 0.19–1.9 lpm), turbine flowmeter 2 (1.9–19 lpm), and rotameter (2.3–23 lpm).

At the glycol fluid temperature $T_g \approx 40°C$, $\Delta p_f - q_i$ re-

Table 1 Measured fluid resistance of inertia track codes A and N; $A_{i1} = A_{i2} = 0.2726$ cm^2

Code	l_i (cm)	l_i/d_i	Δp_f(kPa) – q_i(lpm) relationship	C_{du} Eq. (17)
$A2$	18.6	31.57	$\Delta p_f = 2.064 q_i^2$	0.310
$N2$	5.0	8.49	$\Delta p_f = 0.958 q_i^2$	0.455
$N1$	16.1	27.3	$\Delta p_f = 0.529 q_i^2$	0.612
$A1$	2.5	4.24	$\Delta p_f = 0.305 q_i^2$	0.806

lationships are measured for codes A and N. Table 1 lists the orifice flow relationships generated from measured data by using multiple regression routines, where $A1$ and $N1$ correspond to path $\#i_1$ while $A2$ and $N2$ denote $\#i_2$. Note that the multiple regression and least-squares methods automatically emphasize the region of high q_i. The ultimate discharge coefficient C_{du} is calculated from Eq. (17), where ρ_g is the glycol fluid density.

$$q_i = C_{du} A_i (2\Delta p_f/\rho_g)^{1/2} \tag{17}$$

Next, water is employed as the flow medium in order to examine the parametric effect of T_g on Δp_f, since the effective kinematic viscosity ν_g of the non-Newtonian glycol fluid may ultimately approach unity as T_g is increased. For channel $N1$, Δp_f produced with water is only 10 percent less than that measured with glycol fluid for $q_i = 15$ lpm at 40°C. This is because the effect of T_g on ν_g is not significant; ν_g is 3.6 cSt at 19.4°C and 2.8 cSt at 49°C. Therefore, it can be concluded that the effect of T_g on the overall dynamic response is minor even under hot engine compartment conditions (say, up to 160°C), and this is one of the reasons why the glycol fluid mixture is used for hydraulic mounts.

4 Development of Nonlinear Mathematical Model

A low-frequency mathematical model is developed by combining the lumped parameter governing equations, Eqs. (11)–(13), with nonlinear parameter relationships characterized in Section 3.

4.1 Static Equilibrium Condition. At the static equilibrium, $p_1 = p_2 = \bar{p}$ and $\bar{V}_1 + \bar{V}_2 \approx \bar{V}_2$ since $C_1 \ll C_2$. It follows from Eqs. (9) and (16) that

$$-\bar{F} = A_p(5.26\bar{V}_2^{2.5} - 8.9\times 10^{-5}\bar{V}_2^{6} + 1.41 \times 10^{-5}\bar{V}_2^{6.5}) + \bar{k}_r(\bar{V}_2/A_p)\times 10^{-6} \tag{18}$$

where $\bar{F}$, A_p, $\bar{k}_r$, and $\bar{V}_2$ have the units of N, m^2, N/m and cc, respectively, and $-\bar{x} \approx \bar{V}_2/A_p$ in consistent units. Equation (18) may be solved for $\bar{V}_2$ for a given $\bar{F}$; then $\bar{p}$ is obtained from Eq. (16). Now $\bar{V}_1$ is obtained from Eq. (15). Initial conditions in the mathematical model are given in terms of $\bar{V}_1$, $\bar{V}_2$ and $\bar{p}$ for an applied $\bar{F}$. For instance, $\bar{V}_1 = 0.9920$ cc, $\bar{V}_2 = 28.251$ cc and $\bar{p} = 116.4$ kPa for $A_p = 5.027 \times 10^{-3}$ m^2, $\bar{k}_r = 2 \times 10^5$ N/m and $\bar{F} = -1200$ N.

4.2 Analytical Model. The momentum equations for two parallel paths $\#i_1$ and $\#i_2$ of the inertia track are

$$p_2(t) - p_1(t) = I_{i1}\dot{q}_{i1}(t) + \Delta p_{f1}(t) q_{i1}(t)/|q_{i1}(t)| \tag{19}$$

$$p_2(t) - p_1(t) = I_{i2}\dot{q}_{i2}(t) + \Delta p_{f2})(t) q_{i2}(t)/|q_{i2}(t)| \tag{20}$$

The fluid inertances I_{i1} and I_{i2} of $\#i_1$ and $\#i_2$ are defined as

$$I_{i1} = \rho_g l_{i1}/A_{i1}; \quad I_{i2} = \rho_g l_{i2}/A_{i1} \tag{21a,b}$$

Defining the total fluid volume transferred between chambers #2 and #1 as V,

$$V(t) = \int_0^t [q_{i1}(t) + q_{i2}(t)]dt \tag{22}$$

The volumetric continuity for chamber #2 is expressed by its volume increment V_2 from the condition that $p_2 = p_{atm}$.

$$V_2(t) = \bar{V}_2 - V(t) \tag{23}$$

In consistent units, p_2 is obtained from Eq. (16).

$$p_2(t) = p_2\{V_2(t)\} \tag{24}$$

The volumetric continuity for chamber #1 is represented by its volume increment V_1 from the condition that $p_1 = p_{atm}$.

$$V_1(t) = \bar{V}_1 + V(t) - A_p x(t) \tag{25}$$

When $V_1 > 0$, the top element is compressed and p_1 is obtained in consistent units from Eq. (15). On the other hand, when $V_1 < 0$, it is assumed that $\bar{V}_{air}$ is expanded by an amount equal to $|V_1|$ and p_1 is obtained from the isothermal process.

$$p_1(t) = p_1\{V_1(t)\}, \quad \text{for } V_1(t) > 0 \tag{26a}$$

$$p_1(t) = p_{atm}\bar{V}_{air}/(\bar{V}_{air} + |V_1(t)|), \quad \text{for } V_1(t) < 0 \tag{26b}$$

4.3 Frequency Response. Although the excitation is purely sinusoidal per Eq. (1), the response $F_T(t)$ is nonsinusoidal and asymmetric with respect to the time axis, due to nonlinear system parameters. In the steady state, it may be expressed as below by employing a Fourier series expansion,

$$F_T(t) = F_{T0} + \cdots + \hat{F}_{T1}\sin(\omega t + \phi_1) + \hat{F}_{T2}\sin(2\omega t + \phi_2) + \hat{F}_{T3}\sin(3\omega t + \phi_3) + \cdots \tag{27}$$

where F_{T0} is the mean value, $\hat{F}_{T1}$, $\hat{F}_{T2}$, and $\hat{F}_{T3}$ are the amplitudes of each harmonic, and ϕ_1, ϕ_2, and ϕ_3 are the phase leads of each harmonic with reference to x. The *lower* harmonics are typically negligible. Now, F_{T0} is given as,

$$F_{T0} = \frac{1}{nT_p}\int_0^{nT_p} F_T(t)dt \tag{28}$$

where n = number of cycles of x with period $T_p = 2\pi/\omega$. The Fourier filter algorithm (Doebelin, 1980) is employed in order to extract $\hat{F}_{Tm}$ and ϕ_m ($m = 1, 2, \cdots$) from the nonsinusoidal steady-state response $F_T(t)$, with reference to $x(t)$. The coincident and quadrature components, $\mathcal{P}_m(\omega)$ and $\mathcal{Q}_m(\omega)$, of F_T are given as, where $m = 1, 2, \cdots$,

$$\frac{1}{nT_p}\int_0^{nT_p} \sin m\omega t \cdot F_T(t)dt = \frac{1}{nT_p}\int_0^{nT_p} \sin m\omega t \cdot \hat{F}_{Tm}\sin(m\omega t + \phi_m)dt = \frac{\hat{F}_{Tm}\cos\phi_m}{2} = \mathcal{P}_m(\omega) \tag{29}$$

$$\frac{1}{nT_p}\int_0^{nT_p} \cos m\omega t \cdot F_T(t)dt = \frac{1}{nT_p}\int_0^{nT_p} \cos m\omega t \cdot \hat{F}_{Tm}\sin(m\omega t + \phi_m)dt = \frac{\hat{F}_{Tm}\sin\phi_m}{2} = \mathcal{Q}_m(\omega) \tag{30}$$

It follows that

$$\hat{F}_{Tm}(\omega) = 2\sqrt{\mathcal{P}_m^2(\omega) + \mathcal{Q}_m^2(\omega)} \tag{31}$$

$$\phi_m(\omega) = \tan^{-1}[\mathcal{Q}_m(\omega)/\mathcal{P}_m(\omega)] \tag{32}$$

We may define the displacement-amplitude dependent cross-point dynamic stiffness $K^*(\omega, X)$ in terms of the fundamental harmonic ($m = 1$) as

$$K^*(\omega, X) = K(\omega, X)e^{j\phi_K(\omega, X)} \tag{33}$$

where K and ϕ_K are the dynamic stiffness modulus and loss angle.

$$K(\omega, X) = \hat{F}_{T1}/X; \quad \phi_K(\omega, X) = \phi_1 \tag{34}$$

In order to generate the frequency-domain characteristics of

the hydraulic mount, $K(\omega, X)$ and $\phi_K(\omega, X)$ are calculated at each ω. In a similar way, we may obtain $Q^*_{i1}(\omega, X)$ and $Q^*_{i2}(\omega, X)$, the frequency responses of q_{i1} and q_{i2} with reference to the excitation velocity $\dot{x}(t)$.

$$Q^*_{i1}(\omega,X) = Q_{i1}(\omega,X)e^{j\phi_{qi1}(\omega,X)} \tag{35}$$

$$Q^*_{i2}(\omega,X) = Q_{i2}(\omega,X)e^{j\phi_{qi2}(\omega,X)} \tag{36}$$

where Q_{i1} and Q_{i2} are the fundamental harmonic amplitudes, and ϕ_{qi1} and ϕ_{qi2} are their phase leads.

A direct time domain integration software (ACSL, 1991) is employed to numerically solve all of the governing equations and to implement the Fourier filter algorithm. About five cycles are needed to obtain the steady-state response.

5 Model Verification and Discussion

5.1 Experiment. A hydraulic mount was instrumented to measure $x(t)$, $F_T(t)$ and $p_1(t)$ on a dynamic testing system by employing an LVDT, piezoelectric type dynamic force transducer, and strain-gage type absolute pressure transducer, respectively. The dynamic force transducer can not measure the d.c. component (F_{T0}) (Doebelin,1990); its low frequency limit (−5 percent) is 0.0003 Hz. We should therefore subtract the mean component from the predicted $F_T(t)$ before it is compared with measured $F_T(t)$. However, since $|F_{T0}| \le 0.05|\tilde{F}_{T1}|$ up to 50 Hz, predicted $F_T(t)$ is compared directly with measured $F_T(t)$. The pressure transducer is installed at the side wall of the top element such that its diaphragm is flush with the wall. Its sensing diameter is 6.35 mm; the height of chamber #1 is about 8 mm under $\bar{F} = -1200$ N. Therefore this pressure transducer measures an averaged pressure within chamber #1 essentially, which is compatible with the premise of our lumped-parameter model. The LVDT is already installed inside the hydraulic actuator of the testing system. The highest T_g, measured with a digital thermistor, is 40°C during sinusoidal testing. All signals are acquired by and stored in a two-channel spectrum analyzer, and then transferred to VAX 8500 via a 386SX-PC by employing Standard Data Format utilities program as a communication protocol (Kim, 1992). The results presented here are for the hydraulic mount with channel code N unless specified otherwise, see Table 1.

5.2 Effect of Excitation Frequency. Figure 6 compares measured and predicted $F_T(t)$ at three excitation frequencies $f(=\omega/2\pi)$ with X being maintained as 0.5 mm. The sinusoidal excitation stroke $x(t)$ of the hydraulic actuator is plotted along with $F_T(t)$ in order to show their phase relationship and to assess the extent of nonsinusoidal and asymmetric behavior of F_T. Also, $F_T - x$ Lissajous diagrams are plotted to facilitate the model validation. Such a diagram is useful as already demonstrated by Vliet and Sankar (1983) for the nonlinear analysis of shock absorbers. Its enclosed area is correlated to damping or ϕ_K, and its shape indicates the extent of nonlinearity.

In Fig. 6(*a*) at 7 Hz, prediction matches measurement for both $F_T(t)$ and the $F_T - x$ plots. The phase lead of F_T with respect to x can be observed in the time domain. In Fig. 6(*b*) at 10 Hz, prediction matches measurement reasonably, and the shape of $F_T(t)$ looks triangular. This results from the nonlinear system parameters C_1, C_2, and R_i. In Fig. 6(*c*) at 20 Hz, prediction shows some discrepancy from measurement, which signifies that unmodeled dynamics come into effect. For instance, our model does not predict a large ϕ_K like the experiment. This may be related to the simplifying assumptions made for our low frequency model; it will be explained further.

5.3 Effect of Excitation Amplitude. Figure 7 examines $F_T(t)$ at 15 Hz as X is increased from 0.5 mm to 1.0 mm in a step of 0.1 mm. The enclosed area of the measured $F_T - x$ diagram increases monotonically with X, unlike our model.

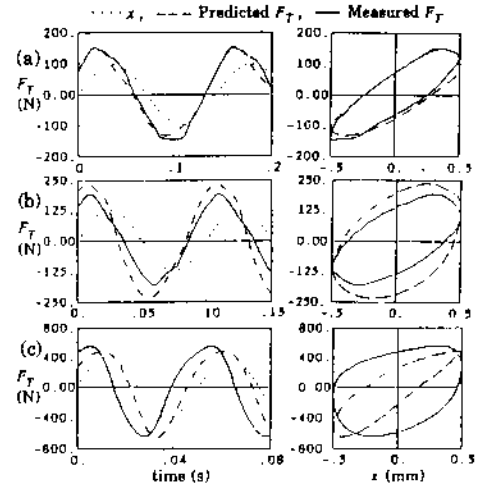

Fig. 6 Effect of excitation frequency on the transmitted force for X = 0.5 mm. (*a*) 7 Hz, (*b*) 10 Hz, (*c*) 20 Hz.

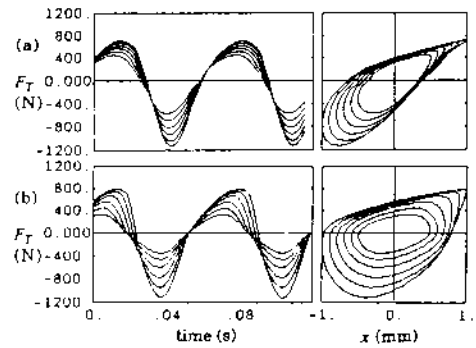

Fig. 7 Effect of excitation amplitude X on transmitted force at 15 Hz. (*a*) Theory, (*b*) experiment.

This discrepancy may be explained as follows. The natural frequency f_n related to the inertia track dynamics, where ϕ_{qi1} and ϕ_{qi2} are around −90 deg, is about 13 Hz for channel code N. As f is increased beyond f_n, ϕ_{qi1} and ϕ_{qi2} approach −180 deg. During the upward x, q_{i1} and q_{i2} flow downward, and some gas may be generated in the upper chamber glycol fluid since p_1 experiences vacuum condition, or even vaporous cavitation may occur when the liquid flow separates from the upper plate. This gas-liquid mixture is associated with C_{12} of Fig. 2(*a*) or specifically the unmodeled negative C_1. Subsequently, when x moves down from the positive peak toward the zero (static equilibrium) position, this gas phase may revert to the liquid state. The volume of generated gas-phase may be a function of t as well as X, as evident from the measured $F_T - x$ diagrams. An accurate modeling of such highly nonlinear and time-varying gas-liquid phase transformation is clearly beyond the scope of this paper. Nonetheless, this unmodeled dynamic phenomenon produces a larger ϕ_K.

5.4 Upper Chamber Pressure. Figure 8 shows $p_1(t)$ and $p_1 - x$ diagram at 15 Hz for X = 0.5 mm. The $p_1 - x$ curve is relatively flat during the upward x, with a minimum p_1 reaching 56.5 kPa (8.2 psia). Since it is still higher than the vapor pressure of glycol fluid (the vapor pressure of H_2O is 15 kPa (2.2 psia) at 54°C), the upper chamber glycol fluid may contain a two-phase mixture. Our model confirms that the upper chamber experiences vacuum condition.

5.5 Frequency Response. The mathematical model is verified in the frequency domain in Fig. 9, where X = 1.0 mm; here the measured dynamic stiffness spectra are for a regular hydraulic mount including a decoupler which is excluded from the model presented here (Kim and Singh, 1992). It is seen

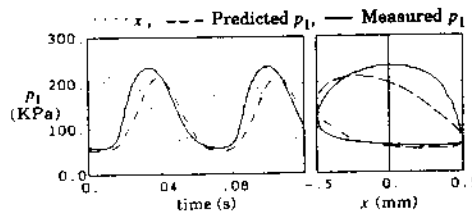

Fig. 8 Upper chamber pressure responses at 15 Hz for X = 0.5 mm

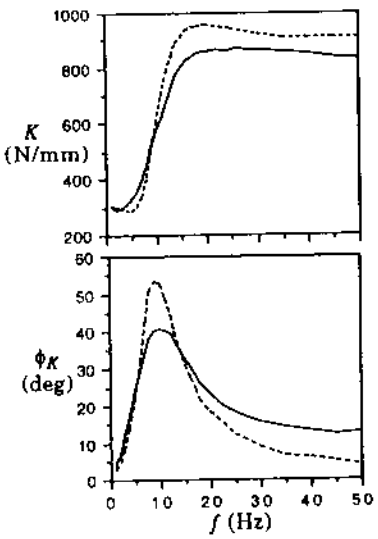

Fig. 9 Dynamic stiffness spectra for X = 1.0 mm; —— experiment for regular mount (inertia track and decoupler), --- theory for inertia track mount

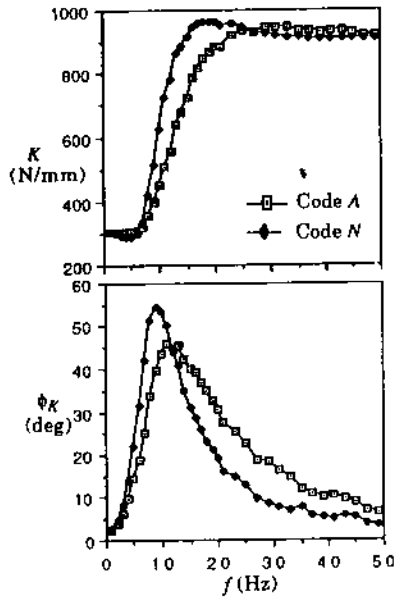

Fig. 10 Effect of inertia track length l_i on the dynamic stiffness spectra; see Table 1 for the specification of inertia track codes

that measured $K(\omega)$ and peak loss angle $\hat{\phi}_K$ are lower than predictions; this discrepancy is due to the decoupler effect of the regular mount. The unmodeled compliance effect of the gas-liquid phase transformation is observed clearly in the plots of $\phi_K(\omega)$; measured ϕ_K becomes larger than the predicted result as f is increased beyond the peak loss angle frequency $\hat{f}_\phi$, toward 50 Hz.

The effect of different channel codes on the mount dynamic properties is shown in Fig. 10, where X = 1.0 mm. As l_{it} becomes shorter from code N to code A, predicted $\hat{f}_\phi$ is increased and $\hat{\phi}_K$ becomes smaller. These trends are also observed in experiment, thus demonstrating that l_i may be varied to tune the engine mounting system.

6 Conclusion

This analytical and experimental study of the low frequency dynamic behavior of a generic hydraulic engine mount with an inertia track has made a number of contributions to the state-of-the-art. First, mount nonlinearities have been identified. Second, new dedicated experimental methods have been developed to characterize nonlinear chamber compliance and fluid resistance parameters. Third, a nonlinear mathematical model has been developed for the first time and verified over the frequency range from 1 to 50 Hz. Fourth, complicating issues such as the generation and collapse of gas-phase and the effect of temperature on the mount dynamic properties have been clarified. Finally, on a fundamental note, our study enriches the literature on nonlinear hydraulic systems. Still, a few research issues remain unresolved. For instance, an accurate model of the gas-liquid phase transformation and cavitation is needed for a better prediction beyond the inertia track natural frequency. However, a rigorous analysis of the transient two-phase flow dynamics is not possible at present. Also, as the excitation frequency is increased, the unsteady-state nature of the inertia track resistance should become significant; however, the measurement of sinusoidal turbulent flow resistance is very difficult, given the current instrumentation technology.

Acknowledgment

This research has been supported by the Teledyne Industries through its research assistance program and by The Center for Automotive Research at The Ohio State. Technical assistance of K. Winkler, E. Schmidt, W. Cummins, and J. Vance of formerly Teledyne Monarch Rubber Co. and equipment donation by PCB Piezotronics Inc. are gratefully acknowledged.

References

Corcoran, P. E., and Ticks, G. H., 1984, "Hydraulic Engine Mount Characteristics," SAE Paper #840407.

Doebelin,E. O., 1980, *System Modeling and Response: Theoretical and Experimental Approaches*, Wiley, New York, NY.

Doebelin, E. O., 1990, *Measurement Systems: Application Design*, 4th Ed., McGraw-Hill, New York, NY.

Flower, W. C., 1985, "Understanding Hydraulic Mounts for Improved Vehicle Noise, Vibration and Ride Qualities," SAE Paper #850975.

Graf, P. L., and Shoureshi, R., 1988, "Modeling and Implementation of Semi-Active Hydraulic Engine Mounts," ASME Journal of Dynamic Systems, Measurement, and Control, Vol. 10, No. 12, pp. 422-429.

Kim, G., 1992, "Study of Passive and Adaptive Hydraulic Engine Mounts," Ph.D. thesis, The Ohio State University.

Kim, G., and Singh, R., 1992, "Resonance, Isolation and Shock Control Characteristics of Automotive Nonlinear Hydraulic Engine Mounts," *Transportation Systems*, Proceedings of ASME/WAM, DSC-Vol. 44, pp. 165-180.

Kirshner, J. M., and Katz, S., 1975, *Design Theory of Fluidic Components*, Academic Press, New York.

Lang, H., 1977, "A Study of the Characteristics of Automotive Hydraulic Dampers at High Stroking Frequencies," Ph.D. thesis, University of Michigan.

Mitchell and Gauthier Associates, 1991, *Advanced Continuous Simulation Language*, Concord, MA.

Pai, S., 1977, *Two-Phase Flows*, Vieweg, Braunschweig.

Singh, R., Kim, G., and Ravindra, P. V., 1992, "Linear Analysis of an Automotive Hydro-Mechanical Mount with Emphasis on Decoupler Characteristics," *Journal of Sound and Vibration*, Vol. 158, No. 2, pp. 219-243.

Vliet, M. V., and Sankar, S., 1983, "Computer-Aided Analysis and Experimental Verification of a Motorcycle Suspension," ASME *Journal of Vibration, Acoustics, Stress, and Reliability in Design*, Vol. 105, pp. 120-131.